

Tunable SERS Enhancement via Sub-nanometer Gap Metasurfaces

Stephen J. Bauman,* Ahmad A. Darweesh, Miles Furr, Meredith Magee, Christos Argyropoulos, and Joseph B. Herzog



Cite This: <https://doi.org/10.1021/acsami.2c01335>



Read Online

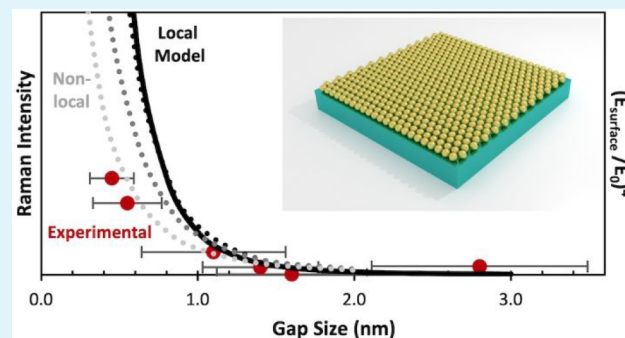
ACCESS |

Metrics & More

Article Recommendations

ABSTRACT: Raman sensing is a powerful technique for detecting chemical signatures, especially when combined with optical enhancement techniques such as using substrates containing plasmonic nanostructures. In this work, we successfully demonstrated surface-enhanced Raman spectroscopy (SERS) of two analytes adsorbed onto gold nanosphere metasurfaces with tunable subnanometer gap widths. These metasurfaces, which push the bounds of previously studied SERS nanostructure feature sizes, were fabricated with precise control of the intersphere gap width to within 1 nm for gaps close to and below 1 nm. Analyte Raman spectra were measured for samples for a range of gap widths, and the surface-affected signal enhancement was found to increase with decreasing gap width, as expected and corroborated via electromagnetic field modeling. Interestingly, an enhancement quenching effect was observed below gaps of around 1 nm. We believe this to be one of the few studies of gap-width-dependent SERS for the subnanometer range, and the results suggest the potential of such methods as a probe of subnanometer scale effects at the interface between plasmonic nanostructures. With further study, we believe that tunable sub-nanometer gap metasurfaces could be a useful tool for the study of nonlocal and quantum enhancement-quenching effects. This could aid the development of optimized Raman-based sensors for a variety of applications.

KEYWORDS: nano-optics, plasmonics, SERS, Raman sensing, subnanometer, metasurface



1. INTRODUCTION

1.1. Background. The proliferation of nanofabrication methods over the past few decades has enabled the study and development of advanced optical technologies such as enhanced sensors. Modern lithographic and self-assembly methods enable the design of nanoscale patterns with the desired material properties.^{1–4} In this field, it is common to make use of the tunable optical properties of plasmonic nanostructures, typically metallic regions with nanoscale dimensions.^{5,6} By controlling the shape and dimensions of such nanostructures, the electron oscillations (plasmons) on the surfaces of the patterns can be tuned to respond optimally to incoming light.^{7–10} Scaling up the effect by creating repeating patterns of plasmonic structures over a surface can enable additional beneficial effects such as tailoring the absorption, reflection, or transmission of light to levels which can be sensed in the lab or implemented in useful technologies.^{11–14}

Optical sensing methods such as Raman spectroscopy make use of light-matter interactions which give a measurable spectral “fingerprint” that can be used to identify the presence and/or concentration of specific molecular species within a sample.¹⁵ Incorporating plasmonic nanostructures into a substrate can enable surface-enhanced Raman spectroscopy

(SERS), whereby designers fabricate structures tuned to the appropriate light wavelength to increase the Raman signal upon scattering by the molecules of interest.^{16–20} This surface enhancement improves the sensitivity of the Raman spectroscopy process, enabling the detection of lower concentrations of the desired analyte.^{21,22} This can also improve the selectivity of Raman spectroscopy by increasing the detectability of the desired molecular species with respect to others in a sample.^{23,24}

While highly repeating patterns of nanostructures aid in increasing their functional area and result in effects associated with the patterns themselves, another strategy can be leveraged to increase signal enhancement by creating plasmonic hotspots—that of introducing nanoscale gaps between adjacent structures.^{25–27} This gap enhancement effect is drastically increased for gaps around and below 10 nm,^{28–33}

Received: January 21, 2022

Accepted: March 16, 2022

and it has been demonstrated for various fabrication strategies and applications, including SERS, at the 1–10 nm scale.^{34–37} Some experimental demonstrations of tunable-gap SERS substrates have even been demonstrated at the sub-20 nm scale.^{38–41} The electric field strength resultant within such nanoscale gaps increases nearly exponentially over this range; hence, for optimal enhancement, the user would desirably produce the smallest possible separation between structures.

One finds, however, that quantum mechanical and other effects begin to limit this local field amplification somewhere in the angstrom-scale gap range.^{42–47} Due to limitations in fabrication processes, there have been few studies of optical signal enhancement for spacings smaller than 1 nm, with most such studies being purely theoretical. There remains a lack of experimental studies on optical signal enhancement versus gap width for small-scale spacings, especially as applied to SERS. Probing the limits of gap width-induced optical enhancement effects can help provide a better understanding of both the physical mechanisms at work and of the optimal fabrication and implementation methods for the development of SERS sensing technology. This work therefore made use of tunable sub-nanometer gap metasurfaces to measure the SERS response versus gap width.

More specifically, in this work, we fabricated and modeled Au nanosphere metasurfaces with tunable gap widths ranging below 1 nm. We studied the local field enhancement within these tunable gaps and experimentally measured surface-enhanced Raman spectra of two analyte molecules adsorbed onto these metasurfaces with a range of gap widths (g). SERS signal intensity measurements were captured versus g for sub-nanometer nanostructure spacings, and these results were compared with theoretical models of optical enhancement versus g . In addition to the standard Drude or “local” model, a “nonlocal” spatially dispersive quantum treatment was incorporated into finite element models for angstrom-scale plasmonic metasurfaces to offer a potential explanation of the experimental behavior.

1.2. Theoretical Considerations for Sub-nanometer Gap Enhancement. Studying plasmonic gap field enhancement at subnanometer length, one reaches gap widths (g) for which quantum or other effects must be considered. Theoretical results predict that the field enhancement does not continue to increase indefinitely at angstrom-scale gap widths.^{47–50} In fact, the enhancement is predicted to plateau and eventually decrease as the gap shrinks below a few angstroms.⁴⁷ This is intuitive, as one at least expects quantum effects to become significant at some angstrom-scale gaps at which one can hardly consider the interatomic spacing to be a plasmonically active gap.

The classical Drude model, often applied to plasmonic (metallic) materials and nanostructures, considers electrons to be localized at the surface of the metallic structure under study.^{51–53} In this way, the charge density is typically pictured and mathematically treated as being compressed into an infinitesimally thin layer at the surface. However, charge density oscillations are not perfectly confined to the surface as the classic model suggests, but they occur over a volume within the surface of the material. As reported in theoretical developments over the past century, the consideration of electron interactions deeper into the material has the effect of reducing the plasmonic field enhancement.^{54–61} The “non-local” or “nonlocal hydrodynamic” model was developed as a more accurate description, which takes into account electron–

electron repulsion. This repulsion manifests as a pressure in the sea of electrons, which resists compression in the presence of an incident electromagnetic field, leading to a spatially dispersive permittivity model for metals.

The Lorentz oscillator appears in this model as an additional term in the wave equation describing the induced current density J in a metal under the presence of an electric field E oscillating at a frequency ω . This additional consideration is shown in eq 1:

$$\beta^2 \nabla(\nabla J) + (\omega^2 + i\gamma_c \omega)J = i\omega\omega_p^2 \epsilon_0 E \quad (1)$$

Here, the material-dependent plasma frequency ω_p and damping coefficient γ_c are as defined in the conventional Drude formula for the complex frequency-dependent permittivity. However, in this equation, β is an additional constant parameter related to the electron pressure. The pressure term is related to the Fermi velocity, v_F , where the value of β is close to the speed of sound in the Fermi-degenerate plasma of conduction electrons in the metal. The result of including this additional pressure term is that the electric permittivity becomes dependent on the longitudinal depth into the material, making it a function of the incident wave propagation vector k , i.e., spatially dispersive. The complex permittivity then takes on separate transverse (ϵ_T) and longitudinal (ϵ_L) forms, where the transverse form is unchanged from the Drude model and ϵ_L appears as in eq 2:

$$\frac{\widetilde{\epsilon}_L(k, \omega)}{\epsilon_0(\omega)} = 1 - \frac{\omega_p^2}{\omega^2 + i\omega\gamma_c - \beta^2 |k|^2} \quad (2)$$

This adjustment to the dielectric function serves to treat the surface charge layer as a volume charge density with a thickness into the metal determined by $\beta/\omega_p \propto \lambda_{TF}$. Here, the Thomas–Fermi screening length, $\lambda_{TF} = v_F/\omega_p$, is on the order of 1 Å. Thus, subnanometer length scale effects are considered via this additional term within the permittivity. This serves as a semiempirical model which allows for computation of results without direct consideration of electron tunneling or other quantum mechanical effects. In other semiempirical treatments, quantum tunneling currents between adjacent nanostructures are considered as well.⁴⁶ However, prior work has demonstrated that experimental results match closely with the hydrodynamic model reported here with no need for the inclusion of tunneling contributions.^{43,48–50,62} This suggests that, at least for the length scales considered in the previous work—gap widths of approximately 1 Å to 10 nm—the electronic pressure effect dominates the experimental results over any tunneling effects. It is fair to note, however, that for smaller dimensions or different geometries than those considered in the listed works, tunneling may provide a significant contribution that must therefore be considered.

The nonlocal treatment has been formulated and applied to various nanogap geometries and situations, including the modeling of Au metasurfaces as in this work.^{46,60–63} Absorption measurements have been compared with the model, demonstrating a reduced g -dependence of the redshift in absorption below a certain value of g .^{43,62} However, experimental results have yet to demonstrate gap-dependent SERS at sub-nanometer scales.

2. EXPERIMENTAL DETAILS

In this work, we used a self-assembly process to design a tunable nanogap metasurface as outlined previously.^{62,64–67} The process relies

on phase separation of nanoparticles from solution and on surface tension gradients, which aid in depositing the metasurface onto a substrate. Gold nanospheres with diameters of 13.3 ± 0.7 nm (average of TEM measurements) were used to fabricate the samples studied in this work.⁶² See Figure 1 inset for TEM images of such

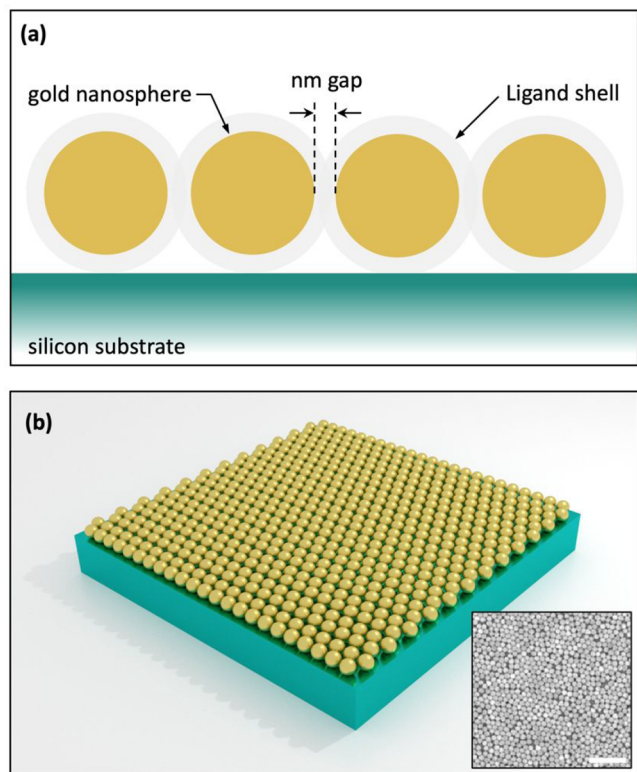


Figure 1. Depiction of Au nanosphere self-assembled metasurface on a Si substrate. (a) Cross-sectional view with Au nanospheres, nanoscale gaps, ligand shells, and Si substrate labeled. (b) 3D schematic of the resulting metasurface (not to scale and zoomed to show Au particles approaching all substrate edges, which may not necessarily occur during fabrication). Inset is a TEM image of a metasurface with 0.55 nm gaps (100 nm scale bar).⁶²

metasurface samples. The Au spheres were in an aqueous suspension at an optical density (OD) $\sim 1 \times 1$ cm (absorption peak) and stabilized in a sodium citrate solution. In a 20 mL scintillation vial, we mixed a solution of 1 mL of tetrahydrofuran (THF) with mono- and dithiol alkane ligands in equal proportions (10 μ L of each).⁶²

The same type of alkyl group for both the thiol and dithiol were mixed for a given solution, and the volume was doubled to 20 μ L for the case of ethanethiols. The Au nanoparticle suspension was mixed into the THF ligand solution. At this stage in the process, ligands bind to the surfaces of the Au nanospheres, displacing the citrate surfactants and causing the spheres to phase-transfer and become hydrophobic. Because THF has a lower density than water, the THF and ligand-coated nanospheres phase separate and the spheres rise to the air–fluid interface, forming a layer atop the liquid surface.

While metasurfaces can be grown along the sides of the vial and removed using a TEM grid (as was done in previous work to obtain gap-width concentrations via TEM imaging)⁶² or other methods, the convenience of metasurface growth directly onto a substrate was utilized for this work. Once the nanoparticle and THF solutions were mixed, $\sim 1\text{--}4$ cm² glass or Si/SiO₂ substrates (previously cleaned in potassium hydroxide dissolved in methanol at a concentration of 5% (w/v)) were placed inside each vial for a given synthesis process, and the vial was shaken vigorously. With the substrates and vial walls wetted by the shaking and/or by deliberate pipetting of solution onto the substrates and the substrates repositioned to be nearly vertical, the deposition of metasurfaces onto these surfaces occurs naturally as follows. The different vapor pressures of THF and H₂O cause the THF to evaporate faster than the water, resulting in a surface tension gradient, which carries the nanoparticles to the vertically oriented surfaces, depositing monolayer films on the substrates and vial walls. The layers formed were macroscopic, substrate-scale metasurfaces of ligand-linked Au nanospheres with the intersphere separation distances controlled by the number of carbons in the alkanethiols. The metasurfaces were left to dry overnight, after which the substrates could be characterized optically. For self-assembly on glass, the regions over which the metasurfaces formed were visibly blue via white light transmission and orange-red via white light reflection. On Si/SiO₂ substrates, film regions appeared a different color than uncoated wafer areas.

The tunability of the metasurfaces comes from the control over the gap size, which is dependent on the choice of alkanethiols used. Previous work has shown that increasing the number of carbons in the ligand molecules results in larger gaps between Au particles throughout the metasurface with relatively high uniformity.^{64,68,69} In

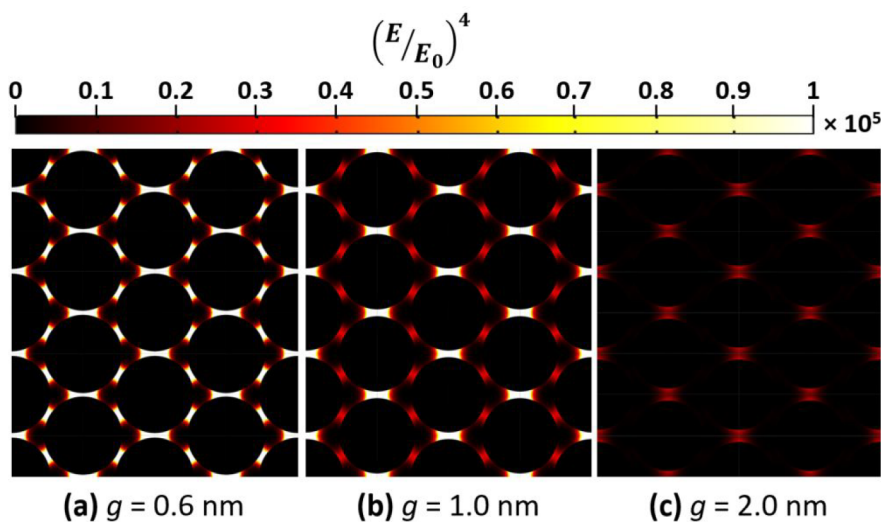


Figure 2. Field enhancement, $\left(\frac{E}{E_0}\right)^4$, distributions for Au metasurfaces with three gap widths, g : (a) 0.6, (b) 1.0, and (c) 2.0 nm. The results are computed using the standard Drude or “local” model.

recent work by the Fontana group, the use of both thiols and dithiols together in the self-assembly process was determined to improve the uniformity and total area of the resulting metasurfaces, as well as improving their mechanical strength, making it possible to transfer them to TEM grids. Nanosphere diameters and gap widths were thereby measured to obtain statistics over large metasurface regions.⁶²

The six different gap widths (and associated thiol mixtures) fabricated and studied in this work include 0.45 ± 0.14 nm (1-ethanethiol/1,2-ethanedithiol), 0.55 ± 0.22 nm (1-propanethiol/1,3-propanedithiol), 1.1 ± 0.46 nm (1-hexanethiol/1,6-hexanedithiol), 1.4 ± 0.37 nm (1-octanethiol/1,8-octanedithiol), 1.6 ± 0.48 nm (1-decanethiol/1,10-decanedithiol), and 2.8 ± 0.69 nm (1-tetradecanethiol/1,14-tetradecanedithiol).⁶²

Figure 1 displays renderings of the type of Au nanosphere self-assembled metasurfaces prepared and studied in this work. Figure 1a shows a cross-section in which can be seen Au nanospheres separated by a nanoscale gap determined by the thickness of the surrounding ligand shell, all on a silicon substrate. Figure 1b shows a three-dimensional (3D) rendering of the same structure, displaying many periods across a large substrate area to better demonstrate the entire metasurface design (not drawn to scale), and the inset is a TEM image of a representative metasurface. The sizes of both the Au nanospheres and the gaps between them can be used to tune the optical response of the metasurface.

2.1. Computational Study. To simulate the optical response of the metasurfaces with different gap widths, we created a three-dimensional finite element model by breaking down the closely packed repeating structure to a reduced unit cell to decrease the computational time. Because of the symmetry of the system, electromagnetic mirror boundary conditions were established so that an infinitely periodic metasurface was simulated by a unit cell containing two quarter spheres with a variable gap width, g . The material properties of the spheres were set to those of pure Au (permittivity values obtained by Johnson and Christy's data)⁷⁰ with the surrounding material set to an effective lossless refractive index ($n = 1.44$) corresponding to that of the alkanethiol ligand shells connecting each sphere. The sphere diameters were set to 13.3 nm to reflect the experiments most accurately. The metasurface layer was modeled as having air above and a lossless glass/SiO₂ substrate layer ($n = 1.53$) below. A linearly polarized 785 nm plane wave was simulated as normally incident upon the metasurface with electric field strength E_0 . We obtained enhancement distributions in the plane bisecting the metasurface by plotting two-dimensional color maps of the field enhancement to the fourth power ($(E/E_0)^4$) where E is the local field strength. The results, shown in Figure 2, were then output by taking a top-down cross-section of the calculated enhancement field distributions for different gap widths. Figure 2 displays the computed enhancement distributions for $g =$ (a) 0.6, (b) 1.0, and (c) 2.0 nm; multiple metasurface periods are shown to aid visualization.

As can be seen in the enhancement distributions, the greatest field strength was localized in the smallest gap regions of the model for all g values. For small gaps, the maximum field region was highly localized in the gap; the high-intensity regions broadened with widening g . Simultaneously, the enhancement rapidly decreased, becoming relatively weak for $g = 2.0$ nm on this fixed color scale.

In the interest of SERS signal enhancement across a larger area of the metasurface, the average enhancement factor, $(E_{\text{surface}}/E_0)^4$, was determined over the entire surface of the Au spheres within the modeled unit cell. This surface-averaged enhancement was obtained for g ranging from 0.2 to 3 nm.

Equation 2 was implemented in the electromagnetic models to study potential nonlocal contributions in the tunable Au metasurfaces due to the extremely small nanogap. This means that the electron interactions within a certain radial distance inside the surface of each Au sphere was considered and found to affect the results, as opposed to infinitesimally thin charge density layers on the spherical surfaces used in the local model. A nonlocal parameter value of $\beta = 1.0 \times 10^6$ m/s is realistic, as demonstrated by prior experiments and theory.⁶³ Additional values of 3.0×10^6 and 5.0×10^6 m/s were used to show the further decrease in enhancement with increasing nonlocal effect

strength. Enhancement results of the local and nonlocal models are plotted later in this manuscript alongside experimental SERS data. Note that the currently presented nonlocal simulation model has been used before⁶² to verify similar gold nanosphere metasurface results.

2.2. Optical Experiments. **2.2.1. Sample Preparation.** Using the previously discussed self-assembly procedure, metasurfaces with a range of reasonably controlled gap widths were fabricated.⁶² Two organic analyte molecules were used mainly because of their well-defined Raman spectra: trans-1,2-bis(4-pyridyl)-ethylene (BPE) and benzenethiol (BZT). Solutions of BPE in ethanol were prepared by weighing BPE in powder form and mixing with ~ 20 mL of ethanol to obtain the desired molarity. Solution molarities from 0.1 to 100 mM were prepared. The metasurface-containing wafers were soaked in the BPE-ethanol solution for at least 45 min, removed, and dried with N₂, resulting in uniform coating across the surface. To coat samples with benzenethiol (BZT), a gaseous phase process was used, due to BZT's high volatility. Each sample was suspended metasurface-side-down above an open 20 mL vial containing BZT solution within a fume hood overnight, allowing the BZT molecules to vaporize and adsorb onto the gold metasurface.

2.2.2. SERS measurements. After the samples were prepared with BPE or BZT, they were placed in the Raman spectroscopy system for optical characterization. Because of the coating methods, it was assumed that BPE and BZT were distributed over the entire silicon chips containing the Au metasurfaces of different gap widths, if not relatively uniformly distributed. The incident laser power at the sample surface was measured to be 52.0 mW with a full width at half-maximum Gaussian beam diameter of approximately 20 μm . For each SERS spectrum obtained from a Au metasurface region on a sample containing adsorbed analyte molecules, a Si background was also measured on the same sample by measuring the spectrum on an area of the substrate where no Au nanosphere layer was present. See Figure 1a in ref 66 for an example of such a Au metasurface fabricated on glass.

3. RESULTS AND DISCUSSION

Figure 3 shows examples of SERS and Si background spectra for a sample containing BPE. As shown, BPE's signature

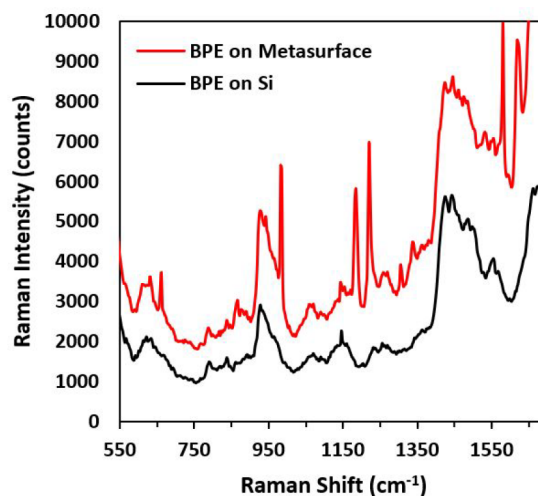


Figure 3. Raw Raman spectra measured at a bare Si region (black) and a Au metasurface region (red) on a sample containing adsorbed BPE.

Raman peaks were not detected for the region of the sample over Si but were significantly enhanced at the metasurface region.

The Si background was subtracted from the SERS signal obtained at each Au monolayer over the range of gap widths

for both BPE and BZT. The results were waterfall plotted for each probe molecule. The SERS spectra for all g values are plotted in Figure 4 for (a) BPE and (b) BZT signals. The

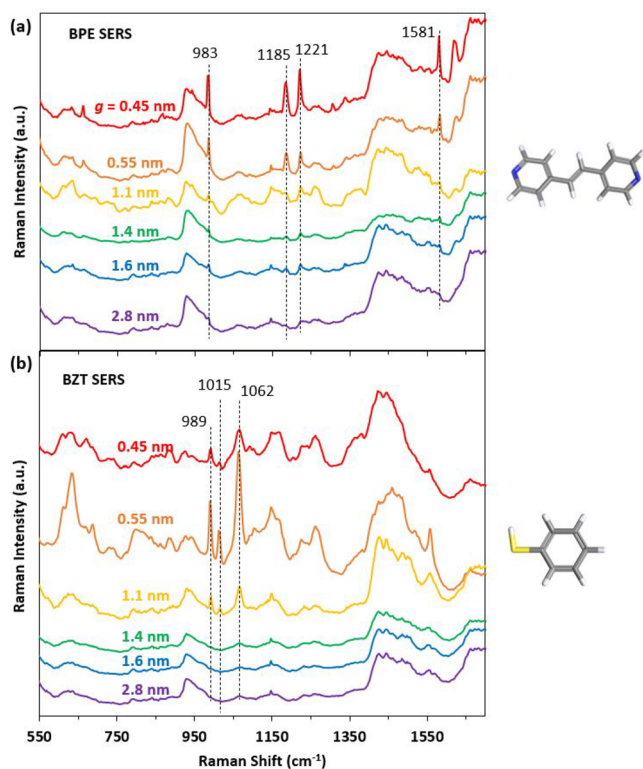


Figure 4. Waterfall-plotted SERS spectra for a range of metasurface gap values from 0.45 to 2.8 nm. Enhanced Stokes shift peaks were observed for samples containing (a) BPE and (b) BZT.

peaks occurring in the SERS spectra correspond to the well-characterized Raman spectra of each analyte. Peaks are labeled in the BPE spectra at 983, 1185, 1221, and 1581 nm; in the BZT spectra, peaks are labeled at 989, 1015, and 1062 nm.

In Figure 4a, the BPE SERS spectra increase in measured intensity for decreasing gap width all the way through $g = 0.45$ nm. The BZT SERS spectra in Figure 4b show the same trend of increasing signal strength with decreasing metasurface gap width up to $g = 0.55$ nm. However, a significant decrease in peak enhancement was observed for the BZT spectra produced by the $g = 0.45$ nm sample (plotted in red). Interestingly, the explanation for this result may correspond to the nonlocal effects that become relevant at length scales close to the ~ 0.5 nm gap width of the self-assembled metasurfaces.

The SERS intensities of one characteristic peak per analyte were plotted versus gap width, with the resulting plots shown in Figure 5. Here, the decrease in enhancement of the BZT SERS signal from $g = 0.55$ nm to $g = 0.45$ nm is more quantitatively illustrated. In both panels a and b in Figure 5, corresponding to BPE and BZT, respectively, the gap width error bars were determined via the standard deviations at each carbon chain length as measured by TEM imaging.⁶² The vertical error bars were based on the noise level in the Raman measurements.

Finally, the experimental SERS results were compared to the computational results for surface-averaged field enhancement versus gap width. The plots shown in Figure 5 combine these computational results with the experimental SERS data for

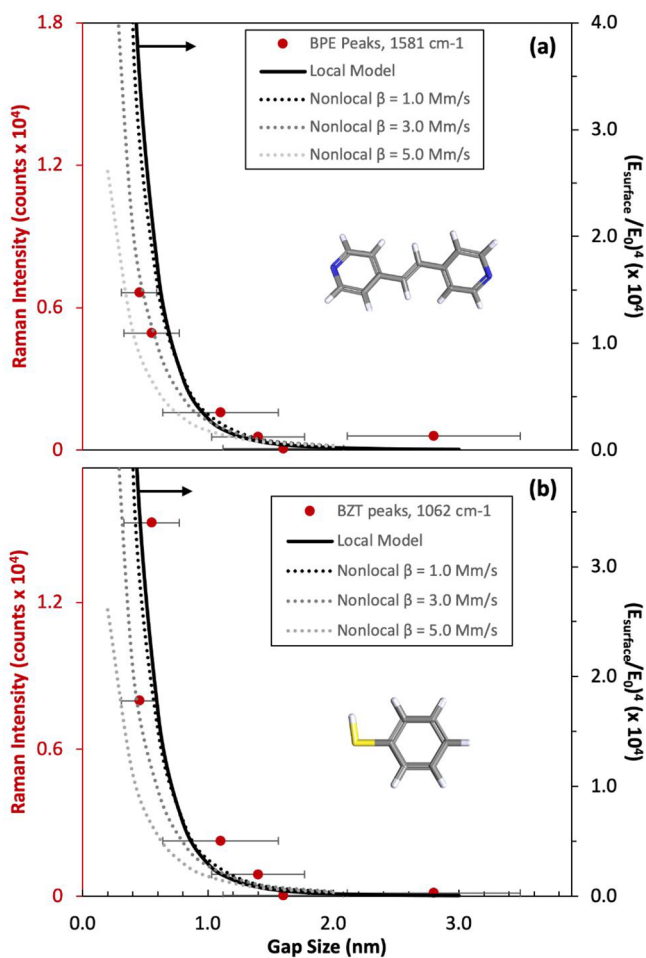


Figure 5. Plots of signal enhancement versus gap width: comparison between experimental SERS on Au metasurfaces (left/red) and theoretical surface enhancement in optical metasurface local and nonlocal models (right/black). Experimental data are shown for (a) BPE and (b) BZT. The results of the local model ($\beta = 0$) and nonlocal models with $\beta = 1.0, 3.0,$ and 5.0×10^6 m/s are plotted as the solid line and increasingly lighter gray dotted lines, respectively.

BPE and BZT spectral peak intensities versus gap width. The BPE and BZT data are shown in panels a and b, respectively, and correspond to the left-hand y -axes that plot the Raman signal intensity. The data plotted here correspond to peak values occurring at Raman shifts of 1581 cm^{-1} for BPE and 1062 cm^{-1} for BZT. The field enhancement calculations based on the classic Drude model, referred to as local, and those based on the nonlocal hydrodynamic model are plotted on the right-hand y -axis as $(E_{\text{surface}}/E_0)^4$. Here, the nonlocal parameter was varied ($\beta = 1.0, 3.0,$ and 5.0×10^6 m/s) for comparison with the experimental Raman intensity data.

An important consideration should be noted regarding the g -dependent increase in SERS signal. In work by Doyle et al., the metasurface absorbance was measured versus gap width (on transparent substrates).⁶² The absorbance peak was found to redshift with decreasing g , an expected plasmon hybridization effect. Interestingly, for the $g = 0.45$ and 0.55 nm metasurfaces, the peak absorbance wavelength had been found to approach 785 nm, the laser wavelength used in the current SERS work. Thus, not only were there likely to be gap-induced field enhancement effects promoting increased SERS at these smaller gap widths, but there was likely to have been a

resonance Raman condition for the same metasurface samples. This effect may have counteracted the nonlocal damping effect, resulting in a less drastic lowering of the SERS signal. More studies will be required to determine the exact nature of the SERS results obtained in this work, including using a shorter probe wavelength to see if stronger SERS occurs for larger gap widths. This would suggest that the resonant wavelength was shifted for larger gap widths, as corresponding to the prior absorption study.^{6,7}

Although the BPE data do not demonstrate a decrease in signal intensity from $g = 0.55$ to 0.45 nm, there is a notable decrease in the rate of increase for this Δg . However, the decrease in signal intensity exists for the BZT data and the same ultrathin gap range. The difference between signal spectra for the two analytes may be due to several factors. Notably, the different molecule deposition methods, soaking in solution versus gas-phase evaporation, may result in different adsorption efficiencies or particle densities over the metasurfaces. Variations in g -distribution across samples or even across sample locations may affect these results, though SERS measurements taken across a given metasurface did not vary significantly. Size and structural differences between BPE and BZT molecules may explain how BZT molecules could adsorb deeper within the hotspot regions, thus allowing them to more readily probe nonlocal plasmonic effects. This could prove to be an important consideration for future studies, especially if BPE has a lower probability of adsorption within gaps below $g = 5$ Å. It is also possible that BZT molecules may more directly affect a decreased enhancement by enabling charge transfer or other plasmon mode hybridization upon entering metasurface gaps.

Regardless, the data suggest that nonlocal or other quenching effects are at least partially responsible for the significant decrease in Raman intensity of BZT and perhaps for the plateauing of the BPE signal. The nonlocal parameter β appears to become an important theoretical inclusion at or below $g \sim 0.5$ nm, and tunneling effects undoubtedly begin to take over below smaller g values. Thus, a hybrid local–nonlocal–tunneling model best explains the presented plasmonic gap field enhancement behavior, where each portion of the model best represents resonance and field enhancement effects over a given range with some overlap. The ability to use optical measurement techniques like SERS to probe these effects, as demonstrated by this work, can serve as an extremely useful tool to experimentally verify theoretical limits going forward.

4. CONCLUSIONS

This work has successfully explored the optical enhancement effects of sub-nanometer gaps down to 0.45 nm for producing increases in signal strength in Raman spectroscopy. Importantly, this is one of the first experimental reports of SERS displaying sub-1 nm gap-width dependence, to the best of our knowledge. Electromagnetic simulations were used to corroborate the experimental results, revealing strong agreement between the two. The results advance the study of plasmonic gap effects by measuring experimental changes in the SERS signal with decreasing gap width for tunable subnanoscale gap metasurfaces. In the case of BZT (the smaller of the two analytes studied), the decrease in SERS signal corresponded with the optical field enhancement limitation described by the nonlocal electron distribution model. The BPE experimental results did not display a field enhancement decrease over the

studied range of gap widths, though the signal increase had begun to plateau for the smaller gap widths probed. Chemical and structural differences between the molecules may be partly responsible for this difference; further work will help to clarify these results by studying additional analyte molecules and using a different wavelength to probe Raman scattering modes. Future work may also incorporate differential spectrum analysis to help reduce the noise background in the signals, improving the comparison between simulations and experimental results.

Overall, the computational trends were found to match the SERS data over the gap widths studied. This demonstrates that precisely tuning the gap width of a plasmonic metasurface is an effective tool for studying Raman signal enhancement. Tunable gap plasmonic metasurfaces were demonstrated as effective and easily fabricated SERS substrates, generating field enhancement on the order of 1×10^4 over measurements on bare Si. This work also adds to the growing field of study of optical enhancement behavior at the angstrom-scale, helping to clarify and confirm existing predictive models. The work also suggests the potentiality of extremely small-gap plasmonics requiring a hybrid nonlocal/quantum model to most accurately describe optical enhancement phenomena at this small scale.

AUTHOR INFORMATION

Corresponding Author

Stephen J. Bauman – *Microelectronics-Photonics Graduate Program, University of Arkansas, Fayetteville, Arkansas 72701, United States*; Present Address: L3Harris Technologies, 2400 Palm Bay Road, Palm Bay, Florida 32905, United States; orcid.org/0000-0003-0891-8839; Email: Stephen.Bauman@l3harris.com

Authors

Ahmad A. Darweesh – *Microelectronics-Photonics Graduate Program, University of Arkansas, Fayetteville, Arkansas 72701, United States*; Present Address: Department of Physics, College of Science, Al-Nahrain University, Baghdad 10072, Iraq; Department of Medical Physics, College of Applied Science, University of Fallujah, Fallujah 31002, Iraq; orcid.org/0000-0003-1062-8558

Miles Furr – *R.B. Annis School of Engineering, University of Indianapolis, Indianapolis, Indiana 46227, United States*; orcid.org/0000-0002-9878-5752

Meredith Magee – *R.B. Annis School of Engineering, University of Indianapolis, Indianapolis, Indiana 46227, United States*; orcid.org/0000-0002-1542-4389

Christos Argyropoulos – *Department of Electrical and Computer Engineering, University of Nebraska-Lincoln, Lincoln, Nebraska 68588, United States*; orcid.org/0000-0002-8481-8648

Joseph B. Herzog – *R.B. Annis School of Engineering, University of Indianapolis, Indianapolis, Indiana 46227, United States*; Department of Physics, University of Arkansas, Fayetteville, Arkansas 72701, United States; orcid.org/0000-0003-2441-6169

Complete contact information is available at: <https://pubs.acs.org/10.1021/acsami.2c01335>

Author Contributions

The manuscript was written through contributions of all authors. All authors have given approval to the final version of the manuscript.

Funding

United States Office of Naval Research Summer Faculty Research Program and Naval Research Enterprise Internship Program (NREIP) and University of Arkansas Microelectronics–Photonics Graduate Program and Department of Physics

Notes

The authors declare no competing financial interest.

ACKNOWLEDGMENTS

S.B. and J.H. extend their appreciation to Jake Fontana and his research team, including specifically Dennis Doyle, at the United States Naval Research Laboratory. They also acknowledge the United States Office of Naval Research for providing research opportunities that enabled this collaborative effort. Specifically, the ONR Summer Faculty Research Program and Naval Research Enterprise Internship Program (NREIP) provided the opportunity to work with the Fontana group during the 2017 and 2018 summers. Work performed by C.A. was supported by the 2017 Office of Naval Research Summer Faculty Research Program.

ABBREVIATIONS

SERS, surface-enhanced Raman spectroscopy; BZT, benzethiol; BPE, trans-1,2-bis(4-pyridyl)-ethylene; TEM, transmission electron microscopy; OD, optical density; THF, tetrahydrofuran

REFERENCES

- (1) Altissimo, M. E-Beam Lithography for Micro-/Nanofabrication. *Biomicrofluidics* **2010**, *4* (2), 026503.
- (2) Biswas, A.; Bayer, I. S.; Biris, A. S.; Wang, T.; Dervishi, E.; Faupel, F. Advances in Top-down and Bottom-up Surface Nanofabrication: Techniques, Applications & Future Prospects. *Adv. Colloid Interface Sci.* **2012**, *170* (1–2), 2–27.
- (3) Bauman, S. J.; Novak, E. C.; Debu, D. T.; Natelson, D.; Herzog, J. B. Fabrication of Sub-Lithography-Limited Structures via Nanomasking Technique for Plasmonic Enhancement Applications. *IEEE Trans. Nanotechnol.* **2015**, *14* (5), 790–793.
- (4) Sun, X.; Li, H. A Review: Nanofabrication of Surface-Enhanced Raman Spectroscopy (SERS) Substrates. *Curr. Nanosci.* **2016**, *12* (2), 175–183.
- (5) Davis, T. J. Plasmonics: The Convergence between Optics and Electronics. *SPIE Proc.* **2013**, 8923, 89232R.
- (6) Gordon, R. Nanostructured Metals for Light-Based Technologies. *Nanotechnology* **2019**, *30* (21), 212001.
- (7) Yamamoto, N.; Ohtani, S.; García de Abajo, F. J. Gap and Mie Plasmons in Individual Silver Nanospheres near a Silver Surface. *Nano Lett.* **2011**, *11* (1), 91–95.
- (8) Edwards, P. R.; Sleith, D.; Wark, A. W.; Martin, R. W. Mapping Localized Surface Plasmons within Silver Nanocubes Using Cathodoluminescence Hyperspectral Imaging. *J. Phys. Chem. C* **2011**, *115* (29), 14031–14035.
- (9) Rodríguez-Oliveros, R.; Sánchez-Gil, J. A. Gold Nanostars as Thermoplasmonic Nanoparticles for Optical Heating. *Opt. Express* **2012**, *20* (1), 621–626.
- (10) Zhang, Y.; Jia, T. Q.; Zhang, S. A.; Feng, D. H.; Xu, Z. Z. Dipole, Quadrupole and Octupole Plasmon Resonance Modes in Non-Concentric Nanocrescent/Nanodisk Structure: Local Field Enhancement in the Visible and near Infrared Regions. *Opt. Express* **2012**, *20* (3), 2924.
- (11) Meinzer, N.; Barnes, W. L.; Hooper, I. R. Plasmonic Meta-Atoms and Metasurfaces. *Nat. Photonics* **2014**, *8* (12), 889–898.
- (12) Chen, W.; Tymchenko, M.; Gopalan, P.; Ye, X.; Wu, Y.; Zhang, M.; Murray, C. B.; Alu, A.; Kagan, C. R. Large-Area Nanoimprinted

Colloidal Au Nanocrystal-Based Nanoantennas for Ultrathin Polarizing Plasmonic Metasurfaces. *Nano Lett.* **2015**, *15* (8), 5254–5260.

(13) Chen, B.; Wood, A.; Pathak, A.; Mathai, J.; Bok, S.; Zheng, H.; Hamm, S.; Basuray, S.; Grant, S.; Gangopadhyay, K.; Cornish, P. V.; Gangopadhyay, S. Plasmonic Gratings with Nano-Protrusions Made by Glancing Angle Deposition for Single-Molecule Super-Resolution Imaging. *Nanoscale* **2016**, *8* (24), 12189–12201.

(14) Bauman, S. J.; Brawley, Z. T.; Darweesh, A. A.; Herzog, J. B. Substrate Oxide Layer Thickness Optimization for a Dual-Width Plasmonic Grating for Surface-Enhanced Raman Spectroscopy (SERS) Biosensor Applications. *Sensors* **2017**, *17* (7), 1530.

(15) Raman, C. V. A New Radiation. *Indian J. Phys.* **1928**, *2*, 387–398.

(16) Jeanmaire, D. L.; Van Duyne, R. P. Surface Raman Spectroelectrochemistry. *J. Electroanal. Chem. Interfacial Electrochem.* **1977**, *84* (1), 1–20.

(17) Kneipp, K.; Moskovits, M.; Kneipp, H. *Surface-Enhanced Raman Scattering: Physics and Applications*; Springer Science & Business Media, 2006.

(18) Lee, S. J.; Guan, Z.; Xu, H.; Moskovits, M. Surface-Enhanced Raman Spectroscopy and Nanogeometry: The Plasmonic Origin of SERS. *J. Phys. Chem. C* **2007**, *111* (49), 17985–17988.

(19) Etchegoin, P. G.; Le Ru, E. C. Basic Electromagnetic Theory of SERS. In *Surface Enhanced Raman Spectroscopy*; Schlücker, S., Ed.; Wiley–VCH, 2010; pp 1–37.

(20) Sharma, B.; Frontiera, R. R.; Henry, A.-I.; Ringe, E.; Van Duyne, R. P. SERS: Materials, Applications, and the Future. *Mater. Today* **2012**, *15* (1–2), 16–25.

(21) Xu, H.; Bjerneld, E. J.; Käll, M.; Börjesson, L. Spectroscopy of Single Hemoglobin Molecules by Surface Enhanced Raman Scattering. *Phys. Rev. Lett.* **1999**, *83* (21), 4357–4360.

(22) Le Ru, E. C.; Etchegoin, P. G. Single-Molecule Surface-Enhanced Raman Spectroscopy. *Annu. Rev. Phys. Chem.* **2012**, *63*, 65–87.

(23) Zhang, X.; Shah, N. C.; Van Duyne, R. P. Sensitive and Selective Chem/Bio Sensing Based on Surface-Enhanced Raman Spectroscopy (SERS). *Vib. Spectrosc.* **2006**, *42* (1), 2–8.

(24) Cottat, M.; D'Andrea, C.; Yasukuni, R.; Malashikhina, N.; Grinyte, R.; Lidgi-Guigui, N.; Fazio, B.; Sutton, A.; Oudar, O.; Charnaux, N.; Pavlov, V.; Toma, A.; Di Fabrizio, E.; Gucciardi, P. G.; Lamy de la Chapelle, M. High Sensitivity, High Selectivity SERS Detection of MnSOD Using Optical Nanoantennas Functionalized with Aptamers. *J. Phys. Chem. C* **2015**, *119* (27), 15532–15540.

(25) Ward, D. R.; Hüser, F.; Pauly, F.; Cuevas, J. C.; Natelson, D. Optical Rectification and Field Enhancement in a Plasmonic Nanogap. *Nat. Nanotechnol.* **2010**, *5* (10), 732–736.

(26) Awang, R. A.; El-Gohary, S. H.; Kim, N.-H.; Byun, K. M. Enhancement of Field-Analyte Interaction at Metallic Nanogap Arrays for Sensitive Localized Surface Plasmon Resonance Detection. *Appl. Opt.* **2012**, *51* (31), 7437–7442.

(27) Li, K.; Jiang, K.; Zhang, L.; Wang, Y.; Mao, L.; Zeng, J.; Lu, Y.; Wang, P. Raman Scattering Enhanced within the Plasmonic Gap between an Isolated Ag Triangular Nanoplate and Ag Film. *Nanotechnology* **2016**, *27* (16), 165401.

(28) Chen, J.; Qin, G.; Wang, J.; Yu, J.; Shen, B.; Li, S.; Ren, Y.; Zuo, L.; Shen, W.; Das, B. One-Step Fabrication of Sub-10-Nm Plasmonic Nanogaps for Reliable SERS Sensing of Microorganisms. *Biosens. Bioelectron.* **2013**, *44*, 191–197.

(29) Tong, L.; Xu, H.; Käll, M. Nanogaps for SERS Applications. *MRS Bull.* **2014**, *39* (02), 163–168.

(30) Gruber, C. M.; Herrmann, L. O.; Olziersky, A.; Puebla-Hellmann, G. F.; Drechsler, U.; Arx, T. von; Bachmann, M.; Koch, M.; Lapin, Z. J.; Venkatesan, K.; Novotny, L.; Lörtscher, E. Fabrication of Bow-Tie Antennas with Mechanically Tunable Gap Sizes below 5 nm for Single-Molecule Emission and Raman Scattering. In *2015 IEEE 15th International Conference on Nanotechnology (IEEE-NANO)*; IEEE: Piscataway, NJ, 2015; pp 20–24.

- (31) Darweesh, A. A.; Bauman, S. J.; Herzog, J. B. Improved Optical Enhancement Using Double-Width Plasmonic Gratings with Nanogaps. *Photonics Res.* **2016**, *4* (5), 173.
- (32) Cai, H.; Wu, Y.; Dai, Y.; Pan, N.; Tian, Y.; Luo, Y.; Wang, X. Wafer Scale Fabrication of Highly Dense and Uniform Array of Sub-5 Nm Nanogaps for Surface Enhanced Raman Scattering Substrates. *Opt. Express* **2016**, *24* (18), 20808.
- (33) Yang, Y.; Gu, C.; Li, J. Sub-5 Nm Metal Nanogaps: Physical Properties, Fabrication Methods, and Device Applications. *Small* **2019**, *15* (5), 1804177.
- (34) Wang, H.-H.; Liu, C.-Y.; Wu, S.-B.; Liu, N.-W.; Peng, C.-Y.; Chan, T.-H.; Hsu, C.-F.; Wang, J.-K.; Wang, Y.-L. Highly Raman-Enhancing Substrates Based on Silver Nanoparticle Arrays with Tunable Sub-10 Nm Gaps. *Adv. Mater.* **2006**, *18* (4), 491–495.
- (35) Mu, C.; Zhang, J.-P.; Xu, D. Au Nanoparticle Arrays with Tunable Particle Gaps by Template-Assisted Electroless Deposition for High Performance Surface-Enhanced Raman Scattering. *Nanotechnology* **2010**, *21* (1), 015604.
- (36) Hatab, N. A.; Hsueh, C.-H.; Gaddis, A. L.; Retterer, S. T.; Li, J.-H.; Eres, G.; Zhang, Z.; Gu, B. Free-Standing Optical Gold Bowtie Nanoantenna with Variable Gap Size for Enhanced Raman Spectroscopy. *Nano Lett.* **2010**, *10* (12), 4952–4955.
- (37) Yokota, Y.; Ueno, K.; Misawa, H. Essential Nanogap Effects on Surface-Enhanced Raman Scattering Signals from Closely Spaced Gold Nanoparticles. *Chem. Commun.* **2011**, *47* (12), 3505–3507.
- (38) Lee, W.; Lee, S. Y.; Briber, R. M.; Rabin, O. Self-Assembled SERS Substrates with Tunable Surface Plasmon Resonances. *Adv. Funct. Mater.* **2011**, *21* (18), 3424–3429.
- (39) Jiwei, Q.; Yudong, L.; Ming, Y.; Qiang, W.; Zongqiang, C.; Wudeng, W.; Wenqiang, L.; Xuanyi, Y.; Jingjun, X.; Qian, S. Large-Area High-Performance SERS Substrates with Deep Controllable Sub-10-Nm Gap Structure Fabricated by Depositing Au Film on the Cicada Wing. *Nanoscale Res. Lett.* **2013**, *8* (1), 437.
- (40) Sun, K.; Meng, G.; Huang, Q.; Zhao, X.; Zhu, C.; Huang, Z.; Qian, Y.; Wang, X.; Hu, X. Gap-Tunable Ag-Nanorod Arrays on Alumina Nanotip Arrays as Effective SERS Substrates. *J. Mater. Chem. C* **2013**, *1* (33), 5015–5022.
- (41) Zhang, C.; Li, C.; Yu, J.; Jiang, S.; Xu, S.; Yang, C.; Liu, Y. J.; Gao, X.; Liu, A.; Man, B. SERS Activated Platform with Three-Dimensional Hot Spots and Tunable Nanometer Gap. *Sens. Actuators B Chem.* **2018**, *258*, 163–171.
- (42) García-Martín, A.; Ward, D. R.; Natelson, D.; Cuevas, J. C. Field Enhancement in Subnanometer Metallic Gaps. *Phys. Rev. B* **2011**, *83* (19), 193404.
- (43) Ciraci, C.; Hill, R. T.; Mock, J. J.; Urzhumov, Y.; Fernández-Domínguez, A. I.; Maier, S. A.; Pendry, J. B.; Chilkoti, A.; Smith, D. R. Probing the Ultimate Limits of Plasmonic Enhancement. *Science* **2012**, *337* (6098), 1072–1074.
- (44) Zhu, W.; Crozier, K. B. Quantum Mechanical Limit to Plasmonic Enhancement as Observed by Surface-Enhanced Raman Scattering. *Nat. Commun.* **2014**, *5*, 5228.
- (45) Yannopapas, V. Quantum Corrections in the Optical Properties of Three-Dimensional Plasmonic Metamaterials with Subnanometer Gaps. *Solid State Commun.* **2015**, *222*, 18–22.
- (46) Zhu, W.; Esteban, R.; Borisov, A. G.; Baumberg, J. J.; Nordlander, P.; Lezec, H. J.; Aizpurua, J.; Crozier, K. B. Quantum Mechanical Effects in Plasmonic Structures with Subnanometre Gaps. *Nat. Commun.* **2016**, *7*, 11495.
- (47) Gordon, R.; Ahmed, A. Reaching the Limits of Enhancement in (Sub)Nanometer Metal Structures. *ACS Photonics* **2018**, *5* (11), 4222–4228.
- (48) Zuloaga, J.; Prodan, E.; Nordlander, P. Quantum Description of the Plasmon Resonances of a Nanoparticle Dimer. *Nano Lett.* **2009**, *9* (2), 887–891.
- (49) Marinica, D. C.; Kazansky, A. K.; Nordlander, P.; Aizpurua, J.; Borisov, A. G. Quantum Plasmonics: Nonlinear Effects in the Field Enhancement of a Plasmonic Nanoparticle Dimer. *Nano Lett.* **2012**, *12* (3), 1333–1339.
- (50) Esteban, R.; Borisov, A. G.; Nordlander, P.; Aizpurua, J. Bridging Quantum and Classical Plasmonics with a Quantum-Corrected Model. *Nat. Commun.* **2012**, *3*, 825.
- (51) Maxwell, J. C., VIII. A Dynamical Theory of the Electromagnetic Field. *Philos. Trans. R. Soc. London* **1865**, *155*, 459–512.
- (52) Drude, P. Zur Elektronentheorie Der Metalle. *Ann. Phys.* **1900**, *306* (3), 566–613.
- (53) Lorentz, H. A. *The Theory of Electrons and Its Applications to the Phenomena of Light and Radiant Heat*; B.G. Teubner: Leipzig, Germany, 1916; pp 1–364.
- (54) Reuter, G. E. H.; Sondheimer, E. H. The Theory of the Anomalous Skin Effect in Metals. *Proc. R. Soc. London Ser. Math. Phys. Sci.* **1948**, *195* (1042), 336–364.
- (55) Dingle, R. B. The Anomalous Skin Effect and the Reflectivity of Metals I. *Physica* **1953**, *19* (1), 311–347.
- (56) Fuchs, R.; Kliewer, K. L. Optical Properties of an Electron Gas: Further Studies of a Nonlocal Description. *Phys. Rev.* **1969**, *185* (3), 905–913.
- (57) Batke, E.; Heitmann, D.; Kotthaus, J. P.; Ploog, K. Nonlocality in the Two-Dimensional Plasmon Dispersion. *Phys. Rev. Lett.* **1985**, *54* (21), 2367–2370.
- (58) Fuchs, R.; Claro, F. Multipolar Response of Small Metallic Spheres: Nonlocal Theory. *Phys. Rev. B* **1987**, *35* (8), 3722–3727.
- (59) García de Abajo, F. J. Nonlocal Effects in the Plasmons of Strongly Interacting Nanoparticles, Dimers, and Waveguides. *J. Phys. Chem. C* **2008**, *112* (46), 17983–17987.
- (60) David, C.; García de Abajo, F. J. Spatial Nonlocality in the Optical Response of Metal Nanoparticles. *J. Phys. Chem. C* **2011**, *115* (40), 19470–19475.
- (61) Fernández-Domínguez, A. I.; Wiener, A.; García-Vidal, F. J.; Maier, S. A.; Pendry, J. B. Transformation-Optics Description of Nonlocal Effects in Plasmonic Nanostructures. *Phys. Rev. Lett.* **2012**, *108* (10), 106802.
- (62) Doyle, D.; Charipar, N.; Argyropoulos, C.; Trammell, S. A.; Nita, R.; Naciri, J.; Piqué, A.; Herzog, J. B.; Fontana, J. Tunable Subnanometer Gap Plasmonic Metasurfaces. *ACS Photonics* **2018**, *5* (3), 1012–1018.
- (63) Toscano, G.; Raza, S.; Jauho, A.-P.; Mortensen, N. A.; Wubs, M. Modified Field Enhancement and Extinction by Plasmonic Nanowire Dimers Due to Nonlocal Response. *Opt. Express* **2012**, *20* (4), 4176–4188.
- (64) Fontana, J.; Maldonado, M.; Charipar, N.; Trammell, S. A.; Nita, R.; Naciri, J.; Pique, A.; Ratna, B.; Gomes, A. S. L. Linear and Nonlinear Optical Characterization of Self-Assembled, Large-Area Gold Nanosphere Metasurfaces with Sub-Nanometer Gaps. *Opt. Express* **2016**, *24* (24), 27360–27370.
- (65) Fontana, J.; Livenere, J.; Bezares, F. J.; Caldwell, J. D.; Rendell, R.; Ratna, B. R. Large Surface-Enhanced Raman Scattering from Self-Assembled Gold Nanosphere Monolayers. *Appl. Phys. Lett.* **2013**, *102* (20), 201606.
- (66) Fontana, J.; Naciri, J.; Rendell, R.; Ratna, B. R. Macroscopic Self-Assembly and Optical Characterization of Nanoparticle-Ligand Metamaterials. *Adv. Opt. Mater.* **2013**, *1* (1), 100–106.
- (67) Bauman, S. J. Optimizing the Plasmonic Enhancement of Light in Metallic Nanogap Structures for Surface-Enhanced Raman Spectroscopy. *Doctoral Dissertation*; University of Arkansas, Fayetteville, Arkansas, 2018.
- (68) Love, J. C.; Estroff, L. A.; Kriebel, J. K.; Nuzzo, R. G.; Whitesides, G. M. Self-Assembled Monolayers of Thiolates on Metals as a Form of Nanotechnology. *Chem. Rev.* **2005**, *105* (4), 1103–1170.
- (69) Martin, J. E.; Wilcoxon, J. P.; Odinek, J.; Provencio, P. Control of the Interparticle Spacing in Gold Nanoparticle Superlattices. *J. Phys. Chem. B* **2000**, *104* (40), 9475–9486.
- (70) Johnson, P. B.; Christy, R. W. Optical Constants of the Noble Metals. *Phys. Rev. B* **1972**, *6* (12), 4370–4379.